A Millimeter-Scale Electric Generator

Matthew K. Senesky[†] and Seth R. Sanders
Department of Electrical Engineering and Computer Science
University of California, Berkeley
Berkeley, CA 94720
[†]Email: senesky@eecs.berkeley.edu

Abstract— **The research presented in this paper concerns the design, construction and testing of an electrical generator intended for interface with a MEMS internal combustion (IC) Wankel engine. The engine and generator are integrated into a single unit by utilizing the engine rotor as the generator rotor. The design allows for thermal insulation between the stator and combustion chamber, simple assembly of the engine and generator and excellent utilization of copper in the generator winding. The majority of the generator structure is built from discrete millimeter-scale components, with only the rotor being microfabricated. Prototype construction and testing are described; a peak open-circuit voltage of 2.63 V and a maximum power output of 375 μW at 13.3 kRPM are reported.**

I. INTRODUCTION

As the size and weight of portable electronic devices are increasingly dominated by electrochemical batteries, there is a growing demand for smaller, lighter power systems with outputs ranging from micro-Watts to tens of Watts. At the low end of this range, demand is driven by wireless sensor networks and MEMS robots; at the high end, demand is driven by consumer electronics such as mobile phones and computing, and military applications such as unattended ground sensors, unmanned aerial vehicles, and electronic systems carried by soldiers [1].

The dominant technology for these applications is the electrochemical battery. Of commercially available battery types, lithium-thionyl chloride (Li–SOCl$_2$) has the highest specific energy among primary batteries at present (660 $\frac{\mathrm{Wh}}{\mathrm{kg}}$), while lithium-sulfur (Li–S) leads among secondary batteries (370 $\frac{\mathrm{Wh}}{\mathrm{kg}}$) [2]. An obvious set of candidates for energy storage with higher levels of specific energy are hydrocarbon fuels, long used in transportation applications for just this reason. Octane, for example, has specific energy of 12.3 $\frac{\mathrm{kWh}}{\mathrm{kg}}$ [3], roughly 18 times that of Li–SOCl$_2$ batteries and 33 times that of Li–S batteries. Of course, chemical to thermal, thermal to mechanical, and mechanical to electrical conversion efficiencies must be taken into account in considering hydrocarbon fuels for electricity production. However, a 10% overall conversion efficiency still results in a higher specific energy than the best available batteries.

Several recent research efforts have sought to capitalize on the high specific energy of chemical fuels through the use of internal combustion (IC) engines paired with electrical generators (see [4] or [5] and its references). This approach leverages the specific energy of hydrocarbon fuels as well as the high power density of IC engines. However, producing such a system to run efficiently on the millimeter- or microscale poses considerable challenges in thermal and fluid management, combustion processes, and electromechanical energy conversion.

The contribution of the research presented in this paper is in the design, construction and testing of an electrical generator intended for interface with a MEMS IC engine. The majority of the generator structure is built from discrete millimeter-scale parts, with only the rotor being microfabricated. We believe that this approach offers superior performance as compared to purely microfabricated generators for power outputs on the order of milli-Watts and above — at these power levels, existing microfabrication techniques do not allow for deposition of sufficient volumes of soft magnetic or electrically conductive material.

The IC engine intended as the prime mover for the generator is a microfabricated Wankel engine [3], [6]. The engine and generator are integrated into a single unit by mounting the generator stator to the silicon engine housing, and utilizing the engine rotor as the generator rotor. This is achieved by electroplating nickel-iron poles into the rotor tips. Integration of the engine and generator avoids shaft coupling between the two machines, simplifying assembly of the devices as well as improving the sealing of the engine housing and reducing unwanted heat flow out of the combustion chamber. It also, however, places unique constraints on the generator design as detailed in Section II.

II. DESIGN

The generator configuration shown in Figs. 1 and 2 was developed in response to two major constraints: the unusual Wankel rotor geometry, which is not well suited to a radial flux design; and the high temperature of the combustion chamber (300°C), which makes a permanent magnet rotor impractical. The generator could be described as an axial flux circumferential current (AFCC) permanent magnet machine, although we note significant differences with the design presented in [7]. The configuration might best be described as an axial-flux claw-pole stator machine, not unlike radial flux designs with concentrated windings presented in [8] and [9]. The stator is a six-pole, single-phase configuration, with the permanent magnet being part of the stator assembly. The flanged triangular rotor (shown in Fig. 3) has a soft magnetic pole in each of its three tips. The design allows for thermal insulation between the stator and combustion chamber, and places the permanent

0-7803-8486-5/04/$20.00

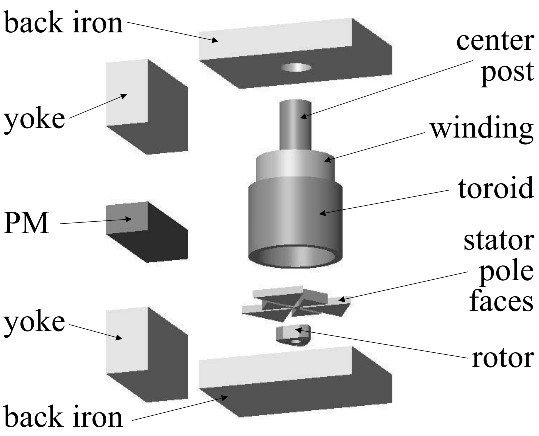

Fig. 1. Generator assembly (engine housing suppressed for clarity).

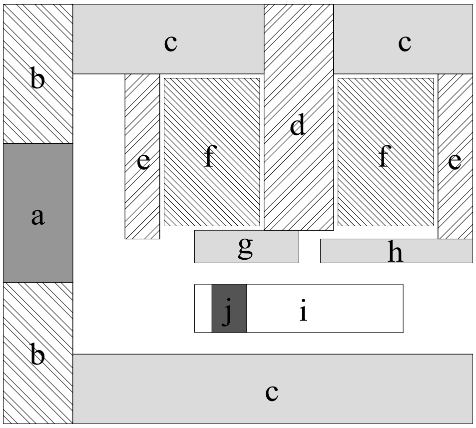

Fig. 2. Schematic cross-section (not to scale). Part names and materials are given below.

a.	Permanent magnet	Bonded NdFeB
b.	Magnet yoke	Low-carbon steel
c.	Back iron	Powdered iron
d.	Center post	Silicon Steel
e.	Toroid	Silicon Steel
f.	Winding	Copper
g.	Center-connected pole face	Powdered iron
h.	Edge-connected pole face	Powdered iron
i.	Rotor	Silicon
j.	Rotor pole	Nickel-iron

magnet in a relatively low temperature location. The axial flux configuration is insensitive to the shape of the rotor poles, and allows simple assembly by sandwiching the engine housing between the upper and lower halves of the stator. The winding arrangement provides for excellent utilization of copper — there are no end turns, none of the dimensions of the coil are constrained by the rotor or permanent magnet structures, and the winding resistance is independent of pole number. The inner diameter of the winding is determined only by the saturation and loss properties of the core material, while the outer diameter and length can be varied to meet performance and size criteria.

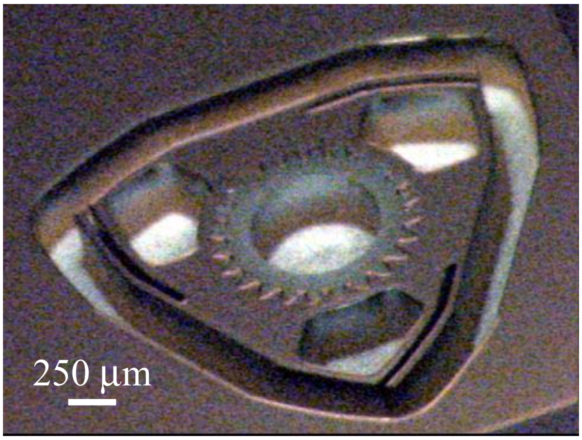

Fig. 3. Microfabricated Wankel rotor, before electroplating.

III. ANALYSIS

Several aspects of the design pose obstacles to straightforward analysis. Flux in the generator travels in three dimensions — axially, radially, and circumferentially. Examination of any one cross section of the machine does not yield a complete picture of the flux paths. Care must be taken in formulating magnetic circuit and finite element models to consider the generator as a three dimensional whole. Note also that the motion of the Wankel rotor includes both rotation and a small eccentricity (i.e. translation in a circular trajectory). Because the eccentricity is much smaller than the rotor radius, the rotor motion is approximated as purely rotational. Perhaps most importantly, the generator is homopolar; the magnetic field in the gap changes in magnitude, but not polarity, as the rotor turns. This implies that performance will be sensitive to saturation of the stator. If the bias field imposed on the stator by the permanent magnet is too large, the low incremental permeability of the stator components will reduce the AC flux linking the coil, resulting in a decrease in power output.

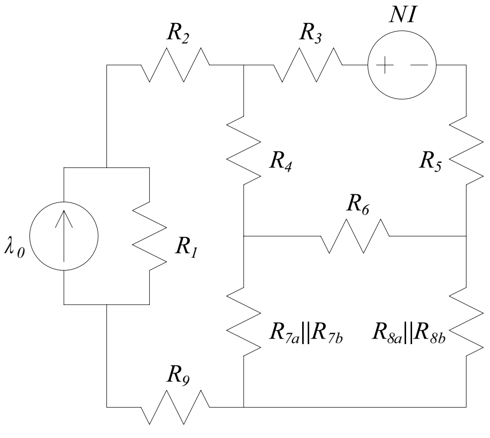

Fig. 4. Magnetic circuit model of the generator.

Figure 4 shows a magnetic circuit model of the generator corresponding to the cross-section of Fig. 2. The permanent magnet is represented by a flux source λ_o in parallel with a leakage reluctance R_1. The winding appears as an MMF source NI. Reluctance R_2 represents the top portion of the magnet yoke; R_3 represents the top portion of the back iron. Reluctance R_4 models the series combination of the toroid and edge-connected pole faces. Similarly, R_5 models the series combination of the center post and center-connected pole faces. The pole to pole leakage path in the stator is represented by R_6. Reluctances R_{7a} and R_{7b} model two paths from the edge-connected pole faces to the lower back iron — one bypassing the rotor poles and one linking the rotor poles, respectively. Similarly, R_{8a} and R_{8b}, model flux paths from the center-connected pole faces to the back iron. Expressions for R_{7a}, R_{7b}, R_{8a} and R_{8b} are given below. Finally, R_9 represents a series combination of the lower back iron and lower magnet yoke, as well as the rotor shaft reluctance when the test rotor described in Section IV is in place.

For the purposes of design, extracting closed-from expressions from a magnetic circuit model with more than five or six elements can be unwieldy. To develop design intuition, a simpler model such as the one shown in Fig. 5 is useful. Here high permeability is assumed in the soft magnetic materials, such that the air gaps dominate the design.

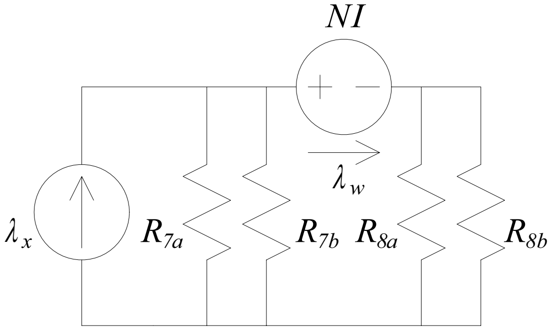

Fig. 5. Simplified magnetic circuit model, assuming high permeability in the soft magnetic components. Expressions for the reluctances are given in Eqs. 1-4

Defining area and length parameters as in Figs. 6 and 7, the reluctances in Fig. 5 can be written as

$$R_{7a} = \frac{\ell_a}{\mu_o(A_z - A_x(1-(\theta\frac{P}{2\pi})))} \quad (1)$$

$$R_{7b} = \frac{\ell_a - \ell_b}{\mu_o A_x(1-(\theta\frac{P}{2\pi}))} \quad (2)$$

$$R_{8a} = \frac{\ell_a}{\mu_o(A_y - A_x\theta\frac{P}{2\pi})} \quad (3)$$

$$R_{8b} = \frac{\ell_a - \ell_b}{\mu_o(A_x\theta\frac{P}{2\pi})} \quad (4)$$

where P is the number of poles, and the rotor angle θ varies from 0 to $\frac{2\pi}{P}$. Note that in this simple model, the parallel combination of all four reluctances does not depend on the rotor position θ, and the leakage reluctance across the permanent magnet is large compared to the gap reluctance. Hence the use of a constant flux source λ_x is justified.

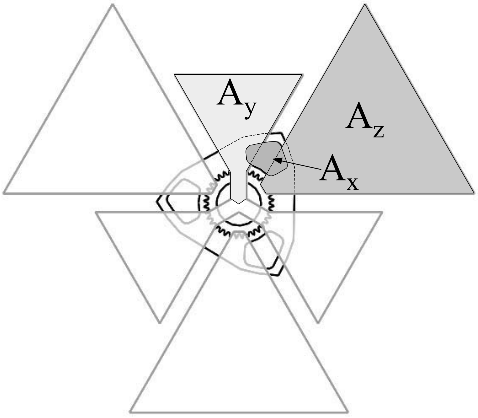

Fig. 6. Pole area parameter definitions. The figure shows a plan view of the stator pole faces and rotor.

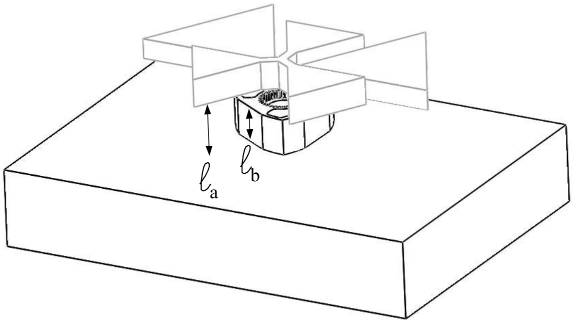

Fig. 7. Length parameter definitions. The figure shows a perspective view of the stator pole faces, rotor, and back iron. Note that one stator pole face has been suppressed for clarity.

From Eqs. 1-4 and Figs. 5-7, the operation of the generator is apparent. As the rotor turns, flux from the permanent magnet is directed either around the outside of the winding, or through its center. This changing flux linkage through the winding generates the back-emf voltage.

Not only is the back-emf voltage intuitive and easy to compute, but it can be shown that for an ideal machine under steady-state conditions, the back-emf constant is equal to the torque constant [10]. Thus torque should be proportional to back-emf per turn, and the back-emf expression reveals a great deal about the design. From Fig. 5 we have

$$\lambda_w = \frac{R_{7a}\|R_{7b}}{(R_{7a}\|R_{7b}) + (R_{8a}\|R_{8b})}\lambda_x, \quad (5)$$

and substituting from Eqs. 1-4

$$\lambda_w = \frac{\ell_b A_x \theta + (\ell_a - \ell_b) A_y}{\ell_b A_x + (\ell_a - \ell_b)(A_y + A_z)} \lambda_x \qquad (6)$$

gives the flux linking the winding (λ_w). Taking the derivative with respect to time gives the back-emf

$$V_o = \frac{\ell_b A_x}{\ell_b A_x + (\ell_a - \ell_b)(A_y + A_z)} \lambda_x \cdot \omega. \qquad (7)$$

Examining Eq. 7, we see that a large ratio of ℓ_b to $(\ell_a - \ell_b)$ (i.e. a small gap) is desirable, as is a rotor pole area A_x that is equal in size to the stator pole areas A_y and A_z.

Using the circuit in Fig. 5, an expression for torque can also be derived. One approach is to calculate the coenergy in the gap, and then take the derivative of coenergy with respect to rotor angle to obtain torque. Note that since the flux in the permanent magnet is assumed to be constant, its contribution to the change in coenergy can be neglected. Coenergy in the soft magnetic components is small due to the materials' high permeability, and is also neglected.

Equation 8 gives an expression for the torque produced by a generator with P poles and winding current NI. The flux density in the rotor due only to the permanent magnet (B_{pm}) is assumed in the model to be independent of rotor position, hence it is simpler to formulate Eq. 8 in terms of this quantity rather than λ_x. The first term in square brackets is the torque due to Lorentz forces, while the second term is due to reluctance forces. For moderate winding currents the reluctance forces are small compared to the Lorentz forces, and the torque can be approximated for initial design purposes by the Lorentz expression only. The absence of a term involving B_{pm}^2 indicates that this model predicts zero cogging torque.

$$\tau = \left[\frac{P^2}{4\pi}\left(\frac{\ell_b}{\ell_a}\right) A_x B_{pm} NI\right] + \left[\frac{\mu_o P^2}{\pi^2}\left(\frac{\ell_b}{\ell_a}\right)\right] \cdot \qquad (8)$$
$$\left[\frac{A_x\{(\ell_a{-}\ell_b(A_y{-}A_z)\pi{+}\ell_b A_x(\theta P{-}\pi)\}}{(\ell_a{-}\ell_b)\{(\ell_a{-}\ell_b)(A_y{+}A_z) + \ell_b A_x\}}(NI)^2\right]$$

Equation 8 gives intuition into the possibility of increasing the torque in the machine. Larger rotor pole area, a thicker rotor, and high flux densities all offer a linear increase in torque. Note however that torque increases with the square of the number of poles. Further, because the generator winding resistance is independent of the pole number, the only limits on the number of poles come from practical limits on the minimum gap size (and hence the pole arc length at which fringing begins to dominate), and higher core loss due to higher electrical frequencies. In the design presented here, a six pole configuration was chosen to coincide with the triangular shape of the Wankel rotor.

While Eqs. 7 and 8 are useful in providing design intuition, an accurate analysis is provided by numerical solution of the detailed magnetic circuit model of Fig. 4, using finite values for R_1, R_2, R_3, R_4, R_5, R_6 and R_9. As noted above, the homopolar nature of the design makes the generator output sensitive to saturation effects. These effects are difficult to calculate by hand; to more accurately model saturation as well as fringing effects, finite element analysis (FEA) can be applied with appropriate saturation characteristics for the soft magnetic materials.

With modest computing resources, nonlinear three-dimensional FEA can be difficult. Hence a series of two dimensional finite element models was developed, as shown in Fig. 8. The figure shows four axisymmetric magnetostatic models, representing cross-sections through two different $r{-}z$ planes of the generator, at two different rotor positions. In Fig. 8a, the cross section is taken through a center-connected pole, with the rotor in an aligned position. Figure 8b shows a cross section through an edge-connected pole at the same rotor position. Figures 8c and 8d show the same cross sections for the complementary rotor position, where the rotor is aligned with the edge-connected pole face.

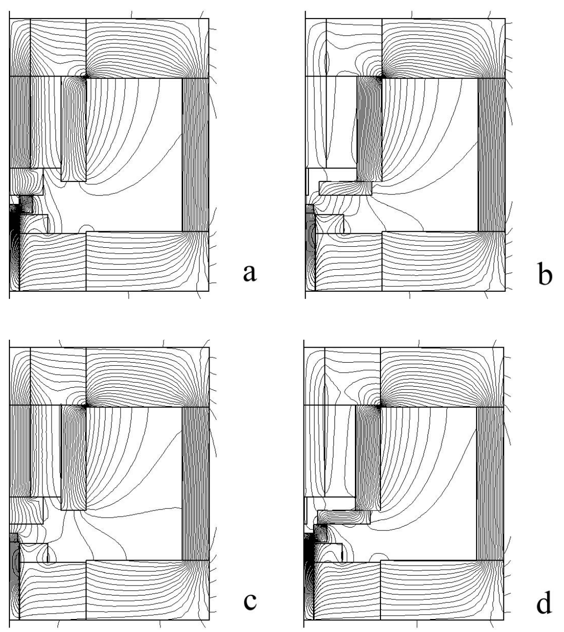

Fig. 8. Axisymmetric finite element models, using the steel test rotor. The left side of each model is the axis of symmetry. Plotted are lines of constant magnetic potential.

From these FEA solutions, values for the relative permeability (μ_r) in each of the soft magnetic components can be determined. Because of their implicit axisymmetry, no one model captures the exact operating point of the generator. However, interpolating between 8a and 8b, and 8c and 8d can give estimates of the level of saturation and appropriate μ_r values for rotor positions $\theta{=}\frac{\pi}{3}$ and $\theta{=}0$ respectively.

Substituting these permeabilities into the magnetic circuit model of Fig. 4, flux linking the winding can be determined for the two rotor positions. Assuming these values to be the maximum and minimum of a sinusoidally varying flux, back-emf can be estimated. Using this method, we calculate a back-emf amplitude of 218 $\frac{\mathrm{nV{\cdot}s}}{\mathrm{rad{\cdot}turn}}$.

IV. CONSTRUCTION

A prototype has been constructed; the upper portion of the stator is shown in Fig. 9. Different soft magnetic materials were used for the various stator components, according to their particular requirements. The stator pole faces are made from powdered iron material (Micrometals' "-26" material [11]). This material was selected for its low loss, high saturation flux density, and isotropic properties. Due to their fine feature sizes, the stator pole faces were formed by electrical discharge machining (EDM). The stator pole faces were positioned with the help of a template, and then potted together with epoxy. The potted stator pole faces are shown in Fig. 10. Powdered iron was also used for the top and bottom portions of the back iron, again due to its low loss and isotropic properties. These pieces were machined with conventional techniques.

Fig. 9. Partial stator assembly, back iron and permanent magnet not shown.

In the center post and toroid portions of the stator, flux distribution is one- or two-dimensional, and high permeability is desired. Sheets of silicon steel (Arnold's "Arnon 5" [12]) 0.005" thick, with magnesium phosphate insulation, were used for these parts. The center post was formed by folding and compressing a single sheet of steel into a layered structure, and then grinding to final shape. The toroid was formed into a roll and secured with epoxy, and the ends were milled to final dimension. Both parts were then etched with dilute nitric acid in a 1:1 ratio of HNO_3:H_2O for 10 seconds to discourage edge-to-edge conduction between laminations. The center post was polished with fine-grain sandpaper before assembly. The finished center post and toroid appear in Figs. 11 and 12 respectively. The winding consists of 4200 turns of 50 AWG wire on a plastic bobbin that encloses the center post and fits inside the toroid.

The permanent magnet was machined from bonded NdFeB ("Neoform" from Dexter Magnetic Technologies [13]) and then magnetized. Due to the sensitivity of the generator design to saturation effects, a fixture was made to hold the permanent magnet and its two yoke pieces. The fixture allows the magnet to be gradually removed from the yoke by turning a screw. Thus the optimal amount of excitation can be determined experimentally.

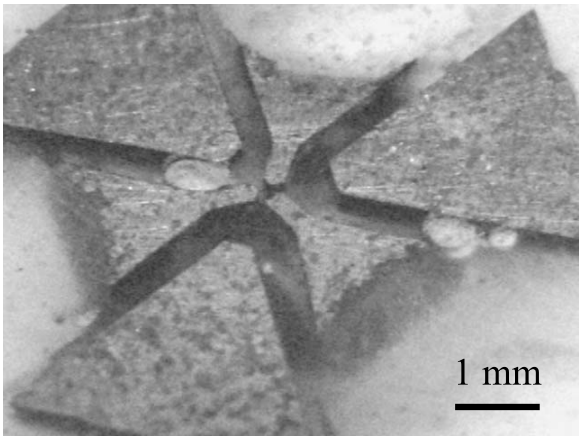

Fig. 10. Powdered iron stator pole faces potted in epoxy.

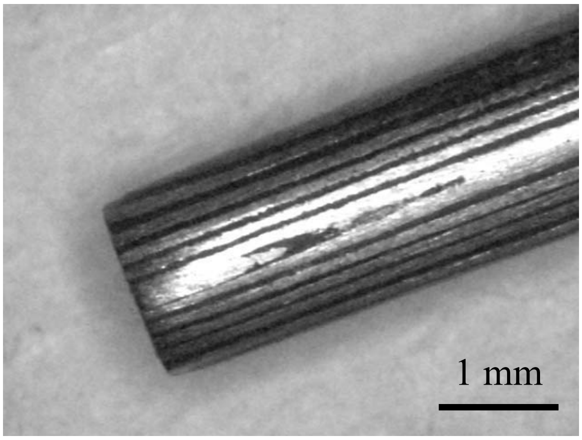

Fig. 11. Laminated silicon steel center post, after etching and polishing.

The silicon rotor was fabricated in the U.C. Berkeley microlab, as described in [14]. The process begins with a 500 μm silicon wafer. Trenches are etched in the shape of the rotor poles. The wafer is then bonded to a second wafer which has a copper seed layer, and the wafer stack is electroplated with a 50:50 ratio of nickel to iron. This composition was selected to satisfy both curie temperature (350° C as given in [15]) and thermal expansion constraints. The top surface of the plated wafer is planarized, the seed wafer is removed, and the remaining features of the rotor are etched using deep reactive ion etching (DRIE).

Because the development of the MEMS Wankel engine has proceeded in parallel with the generator development, an electroplated silicon rotor was not available for generator testing at the time of writing. Hence a solid steel rotor (Fig. 13) was machined with salient pole shapes roughly matching those of the silicon Wankel rotor (Fig. 3). This test rotor has a shaft to allow the spinning of the rotor with an external electric motor.

V. RESULTS

The assembled generator was mounted on a test stand that allows axial adjustment of gap length and lateral adjustment

0-7803-8486-5/04/$20.00 © 2004 IEEE

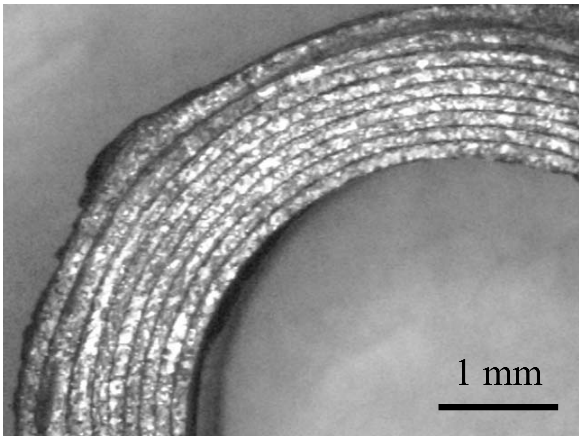

Fig. 12. Laminated silicon steel toroid, after etching.

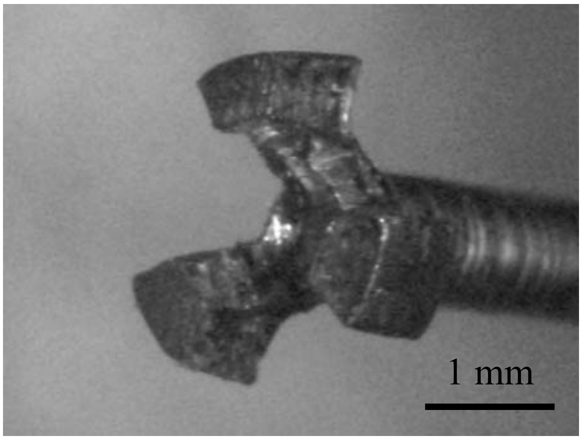

Fig. 13. Steel test rotor. The salient poles are intended to roughly match the size and shape of the pole areas in Fig. 3.

of rotor position. After setting the gap length, lateral position was manually adjusted for maximum back-emf. As described in Sec. IV, permanent magnet excitation was also manually adjusted to maximize back-emf. Resistance and inductance measurements were then made with an LCR meter at 120 Hz and 1 kHz. Measured and calculated values for the winding resistance (R_w), winding inductance (L_w), back-emf constant (K_v), open-circuit voltage (V_o) and maximum power output ($P_{out,max}$) are summarized in Table I.

The nominal speed of operation for the MEMS Wankel engine is a shaft speed of 40 kRPM, corresponding to a rotor speed of 13.3 kRPM, and an electrical frequency of 667 Hz. All the voltage and power measurements reported here were obtained by spinning the steel test rotor with an external DC electric motor at 13.3 kRPM. Because the motor was operated without speed control, variation in the electrical frequency of about 2.5% was observed. In the following, the actual frequency of measurements has been noted where appropriate.

Experimental data showing the open-circuit voltage waveform across the generator terminals appears in Fig. 14. The output has a magnitude of approximately 2.63 V at 677 Hz. The subharmonic content is believed to be due asymmetries in the rotor which cause variations in the waveform once per shaft rotation, or every three electrical periods. A noticeable second harmonic is also present, most likely due to the different shapes of the center-connected and edge-connected stator pole faces.

Quantity	Calculated*	Measured
K_v	218 $\frac{\mathrm{nV\cdot s}}{\mathrm{rad\cdot turn}}$	147 $\frac{\mathrm{nV\cdot s}}{\mathrm{rad\cdot turn}}$
V_o	3.84 V	2.63 V**
R_w	1.92 kΩ	1.95 kΩ†
L_w	76–101 mH	294–310 mH†‡
$P_{out,max}$	947 μW	375 μW♮

* Calculations assume f=667 Hz.
** Measured at 677 Hz. See Fig. 14.
† Measured at 1 kHz.
‡ L_w varies depending on θ.
♮ Measured at f=673 Hz, $\mathrm{R_{load}}$=2.72 kΩ.

TABLE I

Figure 15 shows average power output as a function of load resistance. The plot shows experimental data, as well as a calculated curve based on the measured values in Table I. Because of the frequency variation present in the data, values rescaled to 667 Hz were also plotted, showing the results for constant frequency. The maximum measured power output was 375 μW, achieved at 673 Hz with a load of 2.72 kΩ.

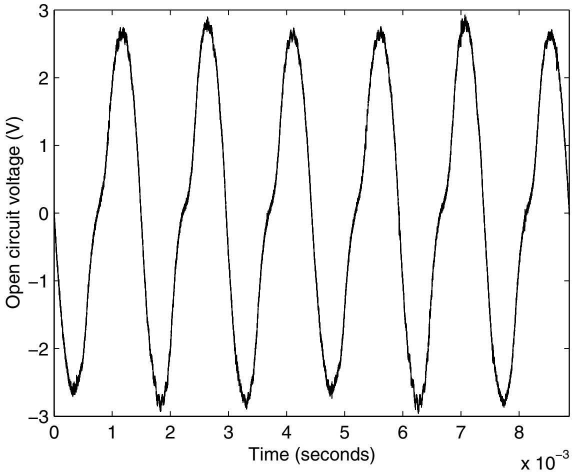

Fig. 14. Open circuit output voltage, f=677 Hz. Peak voltage is approximately 2.63 V.

VI. CONCLUSIONS

A novel electric generator design has been presented. The design is intended to interact with a planar MEMS internal combustion engine, and hence many design choices were guided by the engine configuration. The resulting structure has several interesting features, most notably ample space for windings, and power output that scales with pole number.

The construction of a prototype was described. Experimental results show a peak open circuit voltage of 2.25 V attained

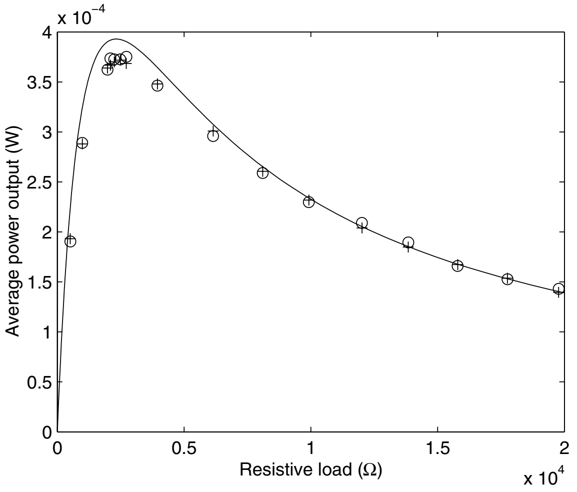

Fig. 15. Average power output versus load resistance. The circles (○) are measured data points, the plus signs (+) are measured data rescaled to account for frequency variation, and the solid line (—) is the calculated result using the measured values from Table I. The maximum measured power output is 375 μW.

at a frequency of 677 Hz, and maximum average power output of 375 μW into a 2.72 kΩ resistive load at 673 Hz.

It is clear that the homopolar nature of the design limited the magnitude of the AC flux linking the stator winding. A similar design with a permanent magnet rotor, having fully reversing flux, should be able to increase this linking flux by more than an order of magnitude. Furthermore, analysis indicates that power output should increase as the square of the number of poles within certain practical limits. Compelling research opportunities exist in the use of the axial-flux claw-pole stator configuration with a high energy product permanent magnet rotor.

ACKNOWLEDGEMENTS

The authors wish to thank DARPA, which supported this work under contract NBCHC010060.

REFERENCES

[1] National Research Council, "Energy-efficient technologies for the dismounted soldier," Technical report, National Academy Press, 1997.

[2] T. R. Crompton, *Battery Reference Book*. Reed Educational and Professional Publishing, 2000.

[3] A. J. Knobloch, "Ultra-deep reactive ion etching for silicon wankel internal combustion engines," Ph.D. dissertation, University of California, Berkeley, 2003.

[4] A. H. Epstein *et al*, "Power MEMS and microengines," in *1997 International Conference on Solid-State Sensors and Actuators (TRANSDUCERS '97)*, vol. 2. IEEE, 1997, pp. 753–6.

[5] A. C. Fernandez-Pello, "Micropower generation using combustion: issues and approaches," in *Twenty-ninth International Symposium on Combustion*, vol. 29. Proceedings of the Combustion Institute, 2002, pp. 883–98.

[6] K. Fu *et al*, "Design and fabrication of a silicon-based MEMS rotary engine," in *2001 ASME International Mechanical Engineering Congress*, vol. 2. ASME, 2001, pp. 3447–52.

[7] J. Luo, D. Qin, T. A. Lipo, S. Li, and S. Huang, "Axial flux circumferential current permanent magnet (AFCC) machine," in *1998 IEEE Industry Applications Conference*, vol. 1. IEEE, 1998, pp. 144–51.

[8] J. Cros, J. R. Figueroa, and P. Viarouge, "BLDC motors with surface mounted PM rotor for wide constant power operation," in *2003 IEEE Industry Applications Conference*, vol. 3. IEEE, 2003, pp. 1933–40.

[9] J. Wang, W. Wang, G. W. Jewell, and D. Howe, "Design optimisation of a miniature multi-pole permanent magnet generator," in *Ninth International Conference on Electrical Machines and Drives*. IEE, 1999, pp. 128–32.

[10] J. R. Hendershot and T. J. E. Miller, *Design of Brushless Permanent-Magnet Motors*. Oxford University Press, 1994.

[11] "Iron powder cores for power conversion and line filter applications," Product catalog, Micrometals, Inc., 2003. [Online]. Available: www.micrometals.com

[12] "Precision rolled strip & foil," Product catalog, Arnold, 2003. [Online]. Available: www.arnoldmagnetics.com

[13] "Neoform material properties," Product data sheet, Dexter Magnetic Technologies, Inc. [Online]. Available: www.dextermag.com

[14] A. J. Knobloch, M. Wasilik, C. Fernandez-Pello, and A. P. Pisano, "Micro internal-combustion engine fabrication with 900 μm deep features via DRIE," in *2003 ASME International Mechanical Engineering Congress*, vol. 5. ASME, 2003, pp. 115–23.

[15] R. M. Bozorth, *Ferromagnetism*. Van Nostrand, 1951.